Three-Dimensional Temperature and Current Distribution in a Battery Module

Mark W. Verbrugge
Physical Chemistry Dept., General Motors Research and Development Center, Warren, MI 48090

A method for treating three-dimensional current and temperature distributions in large-scale battery modules is described. Simulations are presented for a module consisting of cells formed with a lithium metal anode, a polymer electrolyte, and a vanadium oxide cathode. The calculations illustrate the nonlinear dependence of power output on system temperature, which for the investigated lithium-polymer battery module is determined primarily by the influence of temperature on the electrochemical reaction rates and ionic conductivity. An appendix is devoted to the estimation of physicochemical parameters, some of which are not available from the current literature, but are nonetheless important model inputs.

Introduction

Poor heat transfer involving cells in the middle of a large cell stack can lead to substantially nonuniform temperature distributions A detailed knowledge of the system temperature is necessary for understanding power capabilities and materials requirements. Irreversible heating is attributable primarily to resistance associated with mass-transport and electrochemical-kinetics processes. The influence of heat on mass-transport resistance can be understood by recognizing that most liquid-electrolyte transport processes are characterized by an activation energy near 5 kcal/mol (Harned and Owen, 1958). At room temperature, a 5-kcal/mol activation energy will lead to a doubling of electrolyte conductivity for every 25°C temperature increase. A larger spread in activation energies is observed in the electrochemical reactions. The Li-Li^+ reaction relevant to this study has about a 10-kcal/mol activation energy, indicating that for every 10°C temperature increase near room temperature, the interfacial electrochemical kinetic resistance is halved. These resistance changes can have a profound effect on the operation of a battery stack.

The primary contribution of this work is to put forward a method for modeling the transient, three-dimensional (3-D) behavior of a battery system. Distinguishing aspects of this model are the treatment of temperature-dependent system properties commensurate with the above discussion and the calculation of current distributions. The work by Lee et al. (1986) also focused on calculating transient, 3-D temperature profiles but did not account for the influence of temperature on physical properties. The transient, 2-D model by Kim et al. (1992) for a cylindrically symmetric battery treated temperature-dependent thermal properties, but the heat generation rate (resulting from the passage of current) was specified as a model input. Chen and Evans (1993, 1994) provide 2-D analyses of lithium-polymer batteries subject to constant physical properties. The thermal conductivity was treated as orthotropic in the later communication. Thus in these treatments, the current distributions and system power were not influenced by temperature-dependent irreversible processes, in conflict with the above discussion concerning mass-transport and electrochemical-kinetics processes. It is the purpose of this work to complement the previously cited analyses by examining the effect of temperature-dependent physicochemical properties. Agar's review (1963) outlines some of the difficulties associated with the treatment of electrochemical systems containing spatial temperature variations and can be consulted for a discussion of earlier works in this topic area. Reference to other past treatments of thermal models for battery systems can be found in the articles by Lee et al. (1986), Chen and Evans (1993, 1994), and Bernardi et al. (1985), in which a general balance is developed for a battery system in which the temperature is uniform throughout, but changes with time. References to recent 2-D and 3-D modeling investigations of batteries at uniform temperature can be found in the article by Bernardi et al. (1993).

In this communication, model calculations are used to investigate a bipolar cell stack made from cells of the form metallic lithium/polymer electrolyte/vanadium oxide, similar in construction to the bipolar lithium/titanium dioxide battery discussed by Shen and Halpert (1993). It should be emphasized, however, that while an effort has been made to choose representative parameter and property values for the

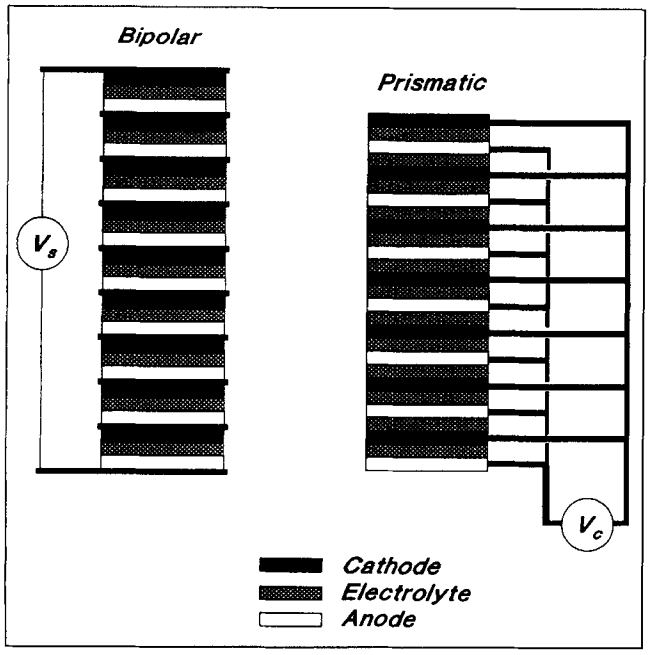

Figure 1. Bipolar stack with 9 cells (left); prismatic arrangement with 7 parallel anodes and cathodes along with 13 electrolyte layers (right).

They are not drawn to scale. (See Table 1 for cell and stack dimensions.)

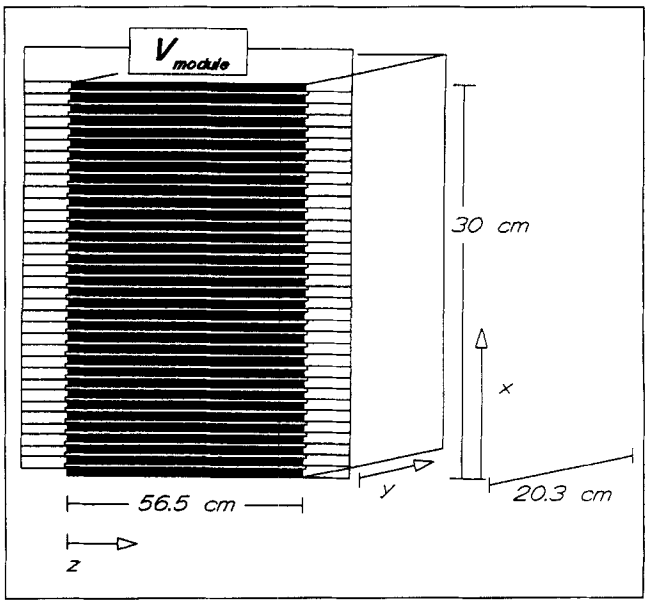

Figure 2. Module formed from 35 bipolar stacks connected in parallel.

$2L_x = 30$ cm, $2L_y = 20.3$ cm, $2L_z = 56.5$ cm. For this work, each stack contains 35 cells.

lithium polymer battery, the main purpose of this work is to propose a method for reducing the physical problem to a set of partial differential equations and demonstrate the utility of the modeling approach by applying it to a system of current interest. In addition to documenting the data and methods used to obtain the needed parameters and properties for the model calculations, the Appendix is useful in terms of elucidating current gaps in the availability of key physical-property data.

The bipolar configuration was chosen for this analysis over that of the prismatic (or monopolar). Both arrangements are shown in Figure 1. Advantages of the bipolar configuration include:

(1) A more uniform current distribution, as the current to each electrode is not drawn off from a cell contact but is allowed to pass across the entire cross-sectional area of the cell.

(2) Less ancillary wiring involved in cell current collecting.

(3) The elimination of electrolyte layers (cf. Figure 1).

The latter two advantages impact energy and power density. The prismatic configuration offers some overcharge protection, as each electrode within a cell experiences the same potential difference. A battery stack formed with prismatic cells, however, must have the cells wired in series to achieve a sufficient stack voltage for high-voltage applications (for example, electric vehicles), which can lead to damaging voltage differences across cells, in the same manner that series connected cells within a bipolar stack can experience excessive voltages. It is possible to monitor the potential of each cell in either arrangement. Shunt currents, resulting from sealing problems at the cell edges, are another concern with the bipolar configuration—polymer electrolytes may help to alleviate such ionic short circuits. The proposed modeling approach for the potential distribution can be altered to describe a prismatic system under certain conditions, as discussed in the context of Eq. 11.

All of the calculations presented in this article are for a battery module, where the term module refers to a battery system formed with bipolar stacks that are connected in parallel. It is important to remember that because of the parallel configuration of the stacks, all of the stacks are maintained at the same voltage V_{stack}. The total current flowing across cells within a stack must be equal, since the cells are connected in series within the stack (Figure 1, left). Since the stacks are connected in parallel, however, to form a module (Figure 2), each bipolar stack acquires a different current due to the nonuniform temperature distribution within the entire module. In particular, the stacks near the center of the module will obtain the largest currents because the center of the module is least accessible for heat rejection to the cooler surroundings, and the higher center temperature decreases transport and kinetic resistances to current flow. In this communication, a module composed of 35 stacks is examined, with each bipolar stack housing 35 cells (1,225 cells per module), as shown in Figure 2.

Governing Equations

Modeling bipolar battery stack

In the derivation to follow, it is assumed that:

(1) No significant concentration gradients develop within the battery system.

(2) The electrochemical reactions can be described by a linear current-potential relation.

(3) There is only one electrochemical reaction at each electrode.

The appropriateness of these assumptions for the purposes of this work is discussed below. It should be recognized that for sufficiently high discharge or charge rates, the first two assumptions can become invalid, and if the discharge or charge rates are extremely high, the solvent can be reacted electrochemically, invalidating the last assumption.

For the lithium polymer battery of this study, the electrode reactions can be written as:

$$Li^+ + e^- \rightleftharpoons Li$$

The first assumption is justified for the electrolyte phase because the current densities of interest are far less than those of the mass-transport-limited value. (See the first equation and related discussion in Jasinski's review, 1971.) Diffusion limitations in the insertion cathode should not be a major concern for the current densities studied in this work. The analysis of Doyle et al. (1993) and Fuller et al. (1994) show that diffusion limitations should not be a factor in typical insertion electrodes. (For example, see Eq. 26 of Doyle et al. (1993). Small values of their dimensionless group S indicate that diffusion resistance within the insertion electrode can be neglected.) The second assumption is valid only near equilibrium, but is often true for the Li-Li^+ reaction far away from equilibrium as well (Odziemkowski, 1992). The cell current densities of interest are usually well below the high exchange current densities for the Li-Li^+ reaction (Verbrugge and Koch, 1994). Thus, low exchange-current-densities values will be employed to represent the current-potential relation, but this is indicative of resistive, ohmic layers formed on the lithium surface, rather than a slow electron-transfer process.

The potential variations in the x direction are addressed first

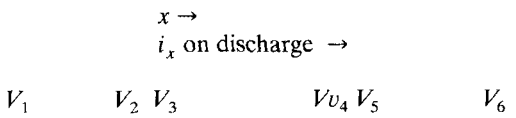

The regions of interfacial reactions correspond to $(V_5 - V_4)$ and $(V_3 - V_2)$. With the stated assumptions, the potential difference across any cell in the battery stack at location (x,y,z) is given by

$$V_{cell}(x,y,z) = (V_6 - V_5) + (V_5 - V_4) + (V_4 - V_3) + (V_3 - V_2) + (V_2 - V_1) = \left[U - i_x \left(\frac{\ell_a}{\sigma_a} + \frac{RT}{i_{oa} nF} + \frac{\ell_e}{\sigma_3} + \frac{RT}{i_{oc} nF} + \frac{\ell_c}{\sigma_c} \right) \right]_{x,y,z} \quad (1)$$

The anode, cathode, and electrolyte layers are denoted by subscripts a, c, and e, respectively. Cell layer thicknesses (in the x direction) are represented by ℓ. Charge conductivity is represented by σ. Exchange current densities are identified by i_o. Faraday's constant, the gas constant, and temperature are given by F, R, and T, respectively. For N cells per unit length x, the potential difference across a differential element of thickness Δx is given by

$$V|_{x+\Delta x} - V|_x = N \times \left[U - i_x \left(\frac{\ell_a}{\sigma_a} + \frac{\ell_c}{\sigma_c} + \frac{\ell_e}{\sigma_e} + \frac{RT}{i_{oa} nF} + \frac{RT}{i_{oc} nF} \right) \right] \Delta x. \quad (2)$$

Dividing by $(\lim_{\Delta x \to 0} \Delta x)$, one obtains:

$$\frac{\partial V}{\partial x} = NU - \frac{i_x}{\sigma_x}, \quad (3)$$

where

$$\frac{1}{\sigma_x} = N \left(\frac{\ell_a}{\sigma_a} + \frac{\ell_c}{\sigma_c} + \frac{\ell_e}{\sigma_e} + \frac{RT}{i_{oa} nF} + \frac{RT}{i_{oc} nF} \right). \quad (4)$$

If the insertion cathode were to be treated as a porous electrode formed by electrolyte and cathode material (Takehara et al., 1991), then the ratio of $[(V_6 - V_5) + (V_5 - V_4)]/i_x$ is still constant and is given by the right side Eq. 43 of the review article by Newman and Tiedemann (1975), and the overall approach is unchanged. Similarly, if multiple reactions are involved wherein each reaction can be described by a linear current-potential relation, then the current-potential relation for the entire interfacial region ($V_5 - V_4$ or $V_3 - V_2$) will be linear. It is also possible to employ nonlinear (Tafel) kinetics using the same overall approach without additional difficulty. More generally, as long as an analytic relationship exists to express the potential differences shown above as a function of the current density i_x and other constants (thicknesses, conductivities, kinetic parameters, and so on), then the derivation provided in this section is not changed significantly.

Potential variations in the y and z directions can be obtained in the same manner, although electrochemical reaction terms no longer apply:

$$-\frac{\partial V}{\partial y} = \frac{i_y}{\sigma_y} \quad \text{and} \quad -\frac{\partial V}{\partial z} = \frac{i_z}{\sigma_z}. \quad (5)$$

Instead of using series resistances appropriate for x-directed current, parallel resistances apply for current passage in the y and z directions. Thus:

$$\sigma_y = \sigma_z = \frac{\ell_a}{\ell}\sigma_a + \frac{\ell_c}{\ell}\sigma_c + \frac{\ell_e}{\ell}\sigma_e, \quad (6)$$

where $\ell = \ell_a + \ell_c + \ell_e$. The governing field equation for the potential is formed by observing current conservation:

$$\nabla \cdot \underline{i} = 0 \quad (7)$$

$$\nabla \cdot (\underline{\underline{\sigma}} \cdot \nabla V) = \frac{\partial}{\partial x}(\sigma_x NU). \quad (8)$$

The charge conductivity tensor is given by

$$\underline{\underline{\sigma}} = \begin{bmatrix} \sigma_x & 0 & 0 \\ 0 & \sigma_y & 0 \\ 0 & 0 & \sigma_z \end{bmatrix}. \tag{9}$$

The component conductivities and the equilibrium potential U are taken to be functions of temperature T only in this work (see Appendix), allowing us to rewrite Eq. 8 in a form convenient for numerical analysis:

$$\sum_{w=x,y,z} \frac{d\sigma_w}{dT}\frac{\partial T}{\partial w}\frac{\partial V}{\partial w} + \sigma_w \frac{\partial^2 V}{\partial w^2} = \left(U\frac{d\sigma_x}{dT} + \sigma_x \frac{\Delta S}{nF}\right)\frac{\partial T}{\partial x}N, \tag{10}$$

where the entropy of reaction term follows from $\Delta S/nF = dU/dT$.

Subject to the stated assumptions, Eq. 10 can be used to treat 3-D potential variations. For the bipolar-stack model of this work, the boundary conditions are

$$\begin{aligned} &x = 0 && V = 0 \\ &x = \mathcal{L}_x && V = V_{\text{stack}} \\ &y = 0 \text{ and } \mathcal{L}_y && \underline{n}\cdot\nabla V = 0 \\ &z = 0 \text{ and } \mathcal{L}_z && \underline{n}\cdot\nabla V = 0 \end{aligned}$$

Thus the stack endplates at $x = 0$ and $x = \mathcal{L}_x$ are taken to be equipotential surfaces, and all other stack surfaces are insulating.

For the specific conditions of this lithium-battery analysis, the electrode conductivities are large enough that equipotential cell endplates yield a variation in potential with x and no appreciable potential variations in y and z. Hence:

$$i_x = -\sigma_x\left(\frac{V_{\text{stack}}}{\mathcal{L}_x} - NU\right), \tag{11}$$

and i_y and i_z are negligibly small. Note that Eq. 11 shows that i_x can vary with position through the temperature dependence of σ_x and U.

Energy balance

By utilizing the first law of thermodynamics for an isobaric battery system, Bernardi et al. (1985) show that

$$Q = I\left(V + \frac{\Delta H}{nF}\right) + MC_p^m\frac{dT}{dt} \tag{12}$$

when the temperature is uniform throughout, enthalpy-of-mixing and phase-change contributions can be neglected, and only one cell reaction prevails. The rate of heat transfer into the battery from the surroundings is given by Q. The battery system's current, voltage, mass, average heat capacity, and temperature are denoted by I, V, M, C_p^m, and T, respectively. On discharge, the battery's current and voltage are positive. The enthalpy of reaction is given by ΔH. Time is represented by t.

It is possible to use Eq. 12 on a differential element in a battery stack to generate the governing partial differential equations. In this macroscopic balance (Bird et al., 1961), the dimensions of the differential element are small relative to the total stack size, but large relative to cell thicknesses. Such a differential balance yields:

$$\begin{aligned} &(i_y\Delta x\Delta z)^2\frac{\Delta y}{\sigma_y\Delta x\Delta z} + (i_z\Delta x\Delta y)^2\frac{\Delta z}{\sigma_z\Delta x\Delta y} \\ &\quad + (q_x^c - q_{x+\Delta x}^c)\Delta y\Delta z + (q_y^c - q_{y+\Delta y}^c)\Delta x\Delta z \\ &\quad + (q_z^c - q_{z+\Delta z}^c)\Delta x\Delta y = (i_x\Delta y\Delta z)\left(V_{x+\Delta x} - V_x + \frac{\Delta H}{nF}N\Delta x\right) \\ &\quad + N\Delta x\Delta y\Delta z\frac{\partial T}{\partial t}\sum_{i=a,c,e}\ell_i\rho_i\hat{c}_{pi}, \end{aligned} \tag{13}$$

where conductive heat fluxes are denoted by q^c. The cell component specific heats (at constant pressure) and mass densities are given by $\hat{c}_{pi}$ and ρ_i (i = anode, cathode, or electrolyte). Note that ohmic heating due to the x-directed current is not stated explicitly as it is included in the current-voltage term. The electrode interfaces are normal to the x coordinate; thus i_y and i_z do not give rise to electrical-work or enthalpy-of-reaction terms. One sees that Q from Eq. 12 corresponds to the left side of Eq. 13, and the right side of Eq. 13 corresponds to the right side of Eq. 12. The governing partial differential equation is formed by dividing both sides of Eq. 13 by $[\lim_{(\Delta x,\Delta y,\Delta z)\to 0}(\Delta x\Delta y\Delta z)]$.

Fourier's heat conduction law,

$$\underline{q}^c = -\underline{\underline{k}}\cdot\nabla T, \tag{14}$$

gives rise to a thermal conductivity tensor $\underline{\underline{k}}$ due to the anisotropic nature of the battery system. Analogous to Eqs. 4 and 6, one can write the thermal conductivities as:

$$\frac{1}{k_x} = N\left(\frac{\ell_a}{k_a} + \frac{\ell_c}{k_c} + \frac{\ell_e}{k_e}\right) \tag{15}$$

$$k_y = k_z = \frac{\ell_a}{\ell}k_a + \frac{\ell_c}{\ell}k_c + \frac{\ell_e}{\ell}k_e. \tag{16}$$

As with the component conductivities, the different cell layers form series resistances to x-directed heat transfer and parallel resistances to heat transfer in the y and z directions, and the thermal conductivity tensor $\underline{\underline{k}}$ corresponds to Eq. 9 with σ's replaced with k's.

Equations 3 and 14 can be substituted into the differential equation resulting from Eq. 13 to yield

$$C\frac{\partial T}{\partial t} = \nabla\cdot(\underline{\underline{k}}\cdot\nabla T) + \underline{\underline{\varrho}}:\underline{i}\,\underline{i} - i_x N\frac{T\Delta S}{nF}. \tag{17}$$

Standard rules for vector algebra are employed (Morse and Feshbach, 1953; Bird et al., 1961). The ohmic heating term corresponds to the double dot product of the charge resistivity tensor $\underline{\underline{\varrho}}$ onto the dyadic product $\underline{i}\,\underline{i}$. The macroscopic

heat capacity C represents $N \sum_{i=a,c,e} \ell_i \rho_i \hat{c}_{pi}$. The almost coordinate-free nature of this equation is appealing, but for simulation purposes it is helpful to rewrite Eq. 17 as

$$C\frac{\partial T}{\partial t} = -i_x N\frac{T\Delta S}{nF} + \sum_{w=x,y,z}\frac{i_w^2}{\sigma_w} + \frac{dk_w}{dT}\left(\frac{\partial T}{\partial w}\right)^2 + k_w\frac{\partial^2 T}{\partial w^2}, \tag{18}$$

where the component conductivities are taken to be functions of temperature, as discussed in the Appendix.

For the bipolar stack model of this work, the initial condition is used to set the system temperature to that of the surroundings:

$$T(0,x,y,z) = T_\infty. \tag{19}$$

The boundary conditions relate thermal conduction at a stack surface to convective heat transfer with the surrounding:

$$w = 0 \quad \text{and} \quad w = \mathcal{L}_w, \quad w = x,y,z, \quad \underline{k}:\underline{n}\nabla T = h(T - T_\infty), \tag{20}$$

where h is a convective heat-transfer coefficient.

Modeling battery modules

The derived potential and energy equations, Eqs. 8 and 17, respectively, are valid for modeling bipolar battery stacks subject to the stated assumptions. Because of the approach taken, it is not necessary to specify the heat evolution rate at individual electrodes, and thermodynamic quantities employed correspond to cell reactions. The difficulties inherent in treating single electrode processes are elucidated in the recent articles by Conway and Wilkinson (1993) and Ratkje et al. (1990), which are concerned with nonisothermal cell potentials and the evaluation of ionic entropies.

For the lithium polymer-electrolyte batteries, the electrodes' electronic conductivities are much larger than the electrolyte's ionic conductivity, i_y and i_z are small relative to i_x, and Eq. 11 is appropriate. When Eq. 11 can be applied, the current density i_x can be taken as a function of temperature only, and the energy-balance Eq. 17 can be applied to a battery module, which is composed of battery stacks that are connected electrically in parallel. That is, the potential difference across each battery stack is identical. Thus for the results discussed in the next section, Eq. 11 is substituted into Eq. 17 to model a battery module. It is assumed that the heat transferred out of the module by the leads that attach to the bipolar stacks is negligible. No resistance to heat transfer is taken into account between the battery stacks forming the module—Eq. 17 applies throughout the module. The boundary conditions 20 stated for the isolated stack are now applied to the surfaces of the module, as is the initial condition 19.

It should be noted that for stacks in which the electrodes are connected in a prismatic manner, as shown in the right of Figure 1, Eq. 11 can be applied if the electrode conductivities are much greater than that of the electrolyte (Verbrugge, 1993). Under such conditions, the thermal characteristics of the bipolar and prismatic stacks are similar. For thermal modeling, the primary difference between the two arrangements is that the thin electronic conductor that separates anodes and cathodes in the bipolar arrangement is replaced by a layer of electrolyte. In addition, there will be some heat transfer out the conductive lead that attaches to each electrode in the prismatic arrangement.

Numerical method

For the module calculations presented in the next section, the energy Eq. 17 was cast in finite-difference form with a truncation error on the order of the square of the mesh spacing (Richtmyer, 1967). The resulting Jacobian matrix contains nonzero diagonals well away from the main diagonal. The effective storage nears that of a square matrix of the order $(njx)(njy)(njz)$, where njx, njy, and njz refer to the number of x, y, and z mesh points, respectively. By taking advantage of the symmetry of the problem, as will be discussed below in the context of Figure 5, the required storage can be reduced substantially. The calculations presented in this work were obtained using a $31\times31\times31$ mesh, yielding better than one percent accuracy for all displayed results. The corresponding number of Jacobian elements nears 10^9. Using eight words per variable, one finds that this corresponds to about 7,000 Megawords. To reduce the storage requirements involved in the direct solution of the matrix equation that results from the finite-difference formulation, Brian's (1961) iterative solution procedure was implemented. The overall procedure for solving the complete problem involved linearizing the equations about a trial solution (Ortega, 1970), casting the equations in finite-difference form, solving the linear-algebra problem using Brian's method, and performing another iteration, if needed, to obtain the solution to the nonlinear problem. Brian's method was taken to be converged when relative change for all elements of the solution vector was less than 10^{-10}.

Results and Discussion

The results generated for this communication were obtained using Eq. 11. The variation in the x-directed current density i_x (Eq. 11), the electrolyte conductivity σ_e (Eq. A4), and the Li-Li$^+$ exchange current density $i_{o,\text{Li-Li}^+}$ (Eq. A5) with temperature is shown in Figure 3. All parameters and properties are specified in Table 1 and are discussed in the Appendix as appropriate. In particular, a wide spread in exchange-current densities for the Li-Li$^+$ reaction has been reported. It is shown in Eq. A7 of the Appendix that

$$i_{oa} + i_{oc} = A\exp\left(-\frac{\Delta H_o}{RT}\right),$$

where the factor A shall be referred to as the cell exchange-current density multiplier, and ΔH_o is the enthalpy of activation at zero polarization for the Li-Li$^+$ reaction. For many of the plots in this section, different values of A are used to demonstrate the influence of electrochemical reaction resistance. The next subsection gives a description of the general character of the calculated results. The following subsection provides sensitivity analyses in terms of predicted module powers and maximum temperatures.

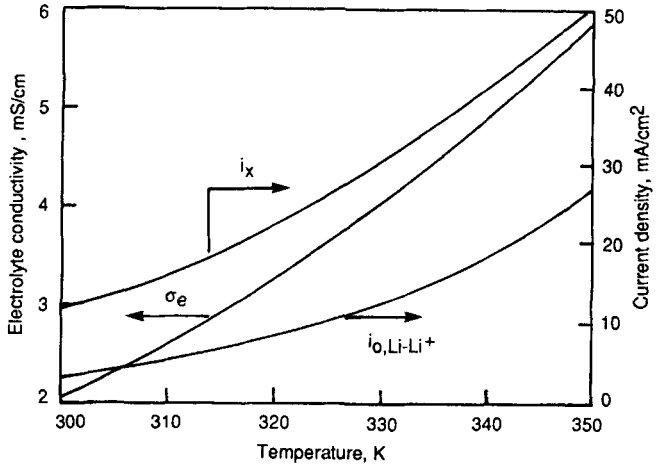

Figure 3. Electrolyte conductivity σ_e, Li-Li$^+$ exchange current density $i_{o,Li\text{-}Li^+}$, and x-directed current density i_x (Eq. 11) as a function of temperature.

General behavior of battery modules

The two quantities of immediate practical interest are the module power and maximum temperature. The total current over a cell at position x, $I(x)$, which also corresponds to the bipolar stack current, is given by

$$I(x) = \int_0^{2L_y}\int_0^{2L_z} i_x\,dz\,dy. \tag{21}$$

The module power can be obtained by integrating the cell currents to obtain the module current, and then multiplying by the module voltage (V_{stack}):

$$\text{Module power} = V_{\text{stack}} \underbrace{\frac{N_{\text{stack}}}{2L_x}\int_0^{2L_x}\int_0^{2L_y}\int_0^{2L_z} i_x\,dz\,dy\,dx}_{\text{Module current}}. \tag{22}$$

The quantity $N_{\text{stack}}dx/2L_x$ represents the number of cell stacks in a differential element of length dx. While the module power allows one to assess the capability of the proposed system for electric-vehicle purposes, for example, the calculated maximum temperature impacts materials-selection decisions and safety concerns. These quantities are shown in Figure 4 for the base case utilizing the parameter and property values presented in Table 1 and the Appendix. Thus the center temperature $T(t,L_x,L_y,L_z)$ and module power (Eq. 22) are plotted against time for different values of the exchange-current density multiplier A (Eq. A7) and different states of charge.

Table 1. Bipolar-Stack Base-Case Values*

A	5.49 kA/cm^2	$\mathcal{L}_z$	56.5 cm
h	0.015 J/cm^2·s·K	$2L_x$	30 cm
ℓ_a	85 μm**	$2L_y$	20.3 cm
ℓ_c	110 μm	$2L_z$	56.5 cm
ℓ_e	50 μm	T_∞	298 K
$\mathcal{L}_x$	0.857 cm	U	2.7 V†
$\mathcal{L}_y$	20.3 cm	$V_{\text{stack}} = V_{\text{module}}$	92 V
		ϵ	0.35

*All other parameters and properties are given in the Appendix. The number of cells per unit length $N = 1/(\ell_a + \ell_c + \ell_e) = 1/\ell = 40.82$ cells/cm, yielding 35 cells/stack. Unless otherwise noted, all plots correspond to 1,800 s of discharge. The number of stacks per module, N_{stack}, is $2L_x/\mathcal{L}_x = 35$.

**One might expect to use commercially available 75-μm-thick lithium (from Foote Mineral); the added 10 μm reflects the properties of the thin electronic conductor placed between the anodes and cathodes (Figure 1).

†Implies 100% state of charge.

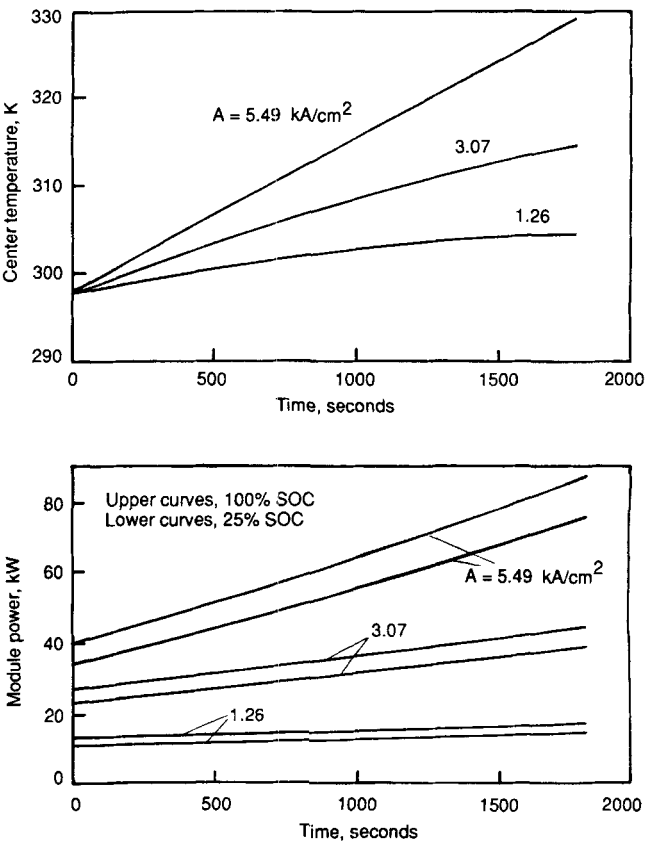

Figure 4. Center temperature $T(t, L_x, L_y, L_z)$ vs. time t (top); module power vs. time (bottom).

The effect of three different exchange-current density multipliers (A, Eq. A7) are investigated; also shown in the lower panel is the effect of state of charge.

From Figure 4, which corresponds to a fixed module voltage, one sees that as heat is evolved during discharge, transport and kinetic resistances are reduced, and higher module currents and powers result with increasing time. Variations in the state of charge (SOC), which result in different open-circuit cell potentials (see Appendix), serve to vertically translate the power vs. time curves. The stack voltages for the different states of charge (100% SOC: $V_{\text{stack}} = 92$ V, 25% SOC: $V_{\text{stack}} = 79.75$ V) were chosen so that $(-NU + V_{\text{stack}}/\mathcal{L}_x)$ were identical for each case, yielding identical i_x values (Eq. 11) and temperature vs. time relations. The curves labeled with $A = 3.07$ kA/cm^2 show about 25 kW of power at 298 K. With four such modules, a 100-kW battery pack results, which is suitable for vehicle applications (Riezenman, 1992; Gosden, 1993).

The temperatures along the three axes of the module are shown in Figure 5 for 600 and 1,800 s of discharge. The temperature profiles correspond to the base case and the rightmost points on the uppermost curves in both panels of Figure

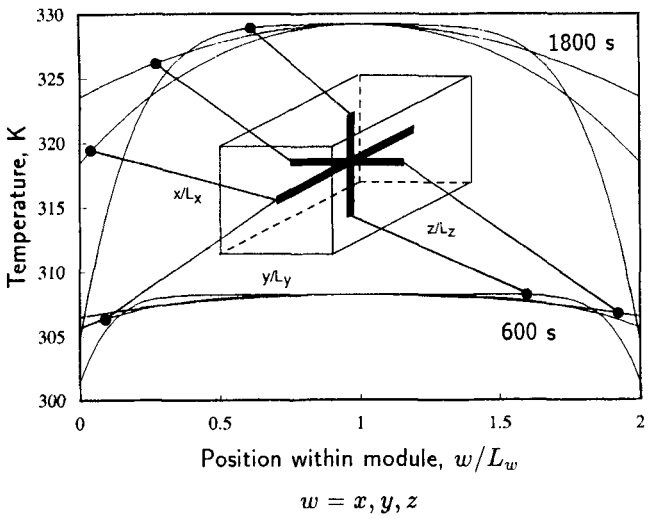

Figure 5. Temperature profiles: $T(t, x, L_y, L_z)$ vs. x/L_x, $T(t, L_x, y, L_z)$ vs. y/L_y, and $T(t, L_x, L_y, z)$ vs. z/L_z.

Upper three curves: $t = 1{,}800$ s; lower three curves, $t = 600$ s. The inset identifies the module axes along which the temperatures are plotted.

4. The x direction maintains the largest resistance to heat conduction, as the cell layers form a series resistance (Eq. 15), and heat must transfer through the lower conductivity polymer electrolyte. The parallel resistance associated with heat transfer in the y and z directions (Eq. 16) allows for the majority of the heat to transport along the electrode materials, which are more conductive than the electrolyte. Thus the temperature gradients are largest along the x axis of the module. The gradients in the y and z directions are similar, as indicated by the profiles of Figure 5 (taking into account that L_z is larger than L_y).

The symmetric nature of the temperature profiles shown in Figure 5 helps to explain the similar symmetry in the plots of the total cell currents (or stack currents, cf. Eq. 21) shown in Figure 6. Equation 21 was used to determine the total current over a cell at position x. The results correspond to the base case and the uppermost curves in Figure 4. Since these currents also correspond to the bipolar stack currents, it is clear that currents drawn from stacks near the center of the module will be much greater than those of the module endplates at $x = 0$ and $2L_x$. The integrated amount of current drawn from the stacks yields the module current, as shown in Eq. 22.

The last figure used to elucidate the general behavior of the battery module is shown in Figure 7. These current density (i_x) surface contours relate to the curve shown in Figure 6 labeled 1,800 s. While the curves in Figure 6 gives the total current passing across a cell vs. the position x, the contours in Figure 7 show the current density $i_x(t,x,y,z)$ over a cell at 1,800 s and three different x positions: $x = 0$, $L_x/2$, and L_x. Only the current density over one-fourth of the cell area is shown; as with the temperature profiles, the current-density contours are symmetric, and displaying the remaining three-fourths of the current-density contour imparts no new information. The schematic to the right of each contour helps to locate the cell surface corresponding to the plotted current density. Note that the current density axis for the uppermost

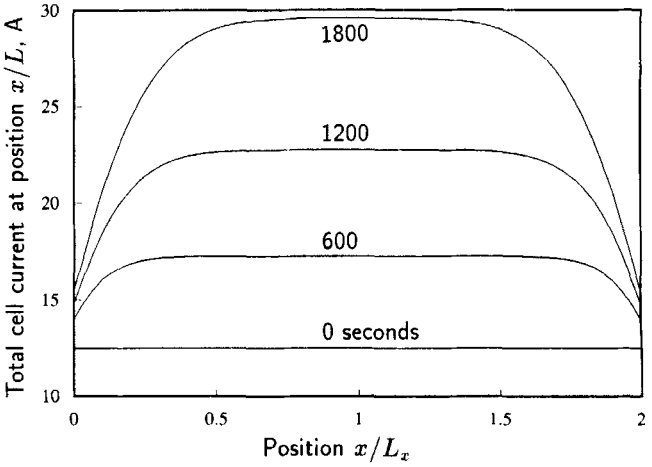

Figure 6. Bipolar stack currents, $I(x)$ vs. x/L_x (Eq. 21).

The different discharge times are listed.

contour differs from that of the middle and lower plots. For all cells in the module, the maximum temperature is at the cell center, and the minimum temperature is at the cell edge contacting the module casing. Because the maximum module temperature is at the module center, and the module's surface temperatures are all near 298 K, the maximum temperature difference is registered across the center cell of the module, located at $x = L_x$. Thus the center cell's current-density contour (lowest panel) shows the highest current density and the largest current-density variation.

Sensitivity analyses

Due to the exponential dependence of both the exchange current density and electrolyte conductivity on temperature,

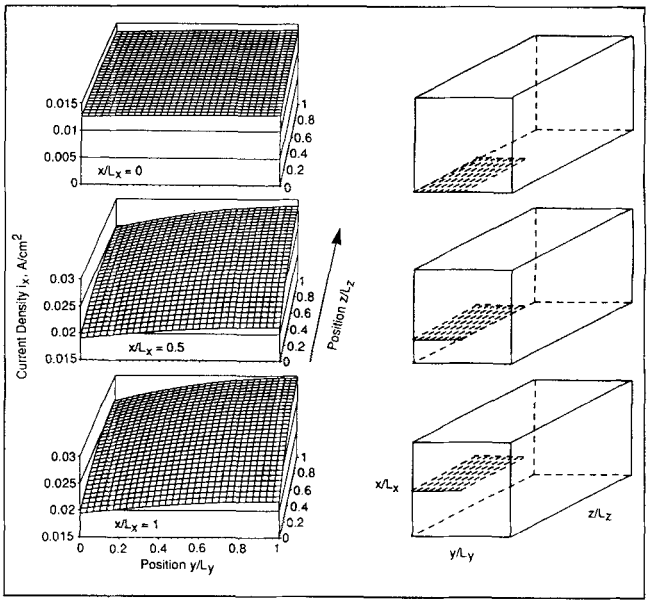

Figure 7. Contours of current density $i_x(t, x, y, z)$.

The module schematic to the right of each contour locates the cell surface corresponding to the plotted current density. The current-density axis for the uppermost contour differs from that of the middle and lower plots. Conditions correspond to those of the uppermost curve in Figure 6.

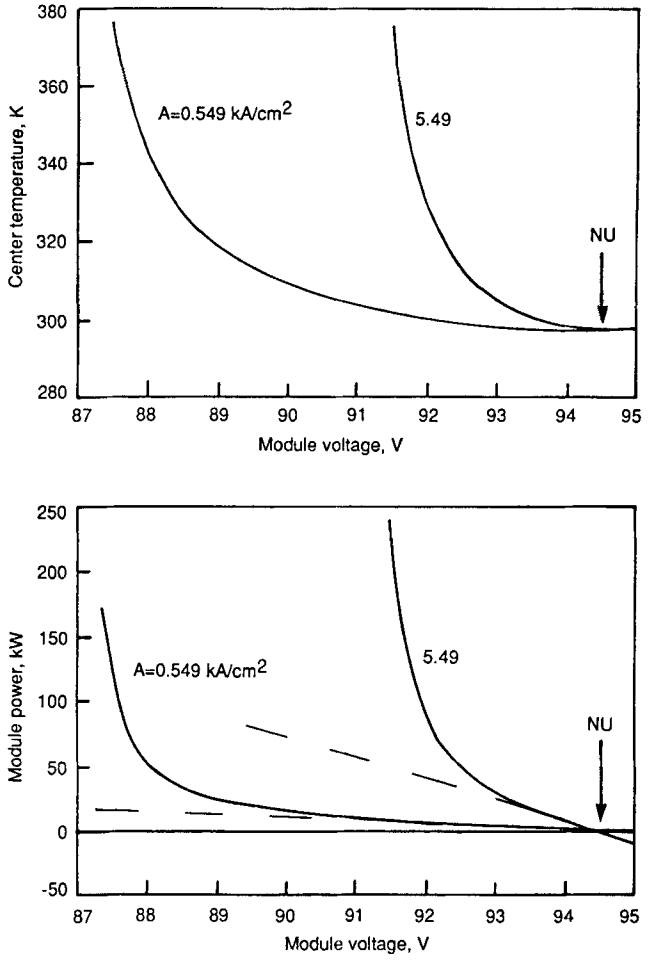

Figure 8. Center temperature and power vs. voltage for two different exchange current density multipliers *A* (Eq. A7).

The module's open-circuit potential at 100 percent state of charge is indicated ($NU = 94.5$ V). These results correspond to the base-case parameter values and 1,800 s into discharge. Calculations using temperature-independent system properties are indicated by the dashed curves (see Eq. 23).

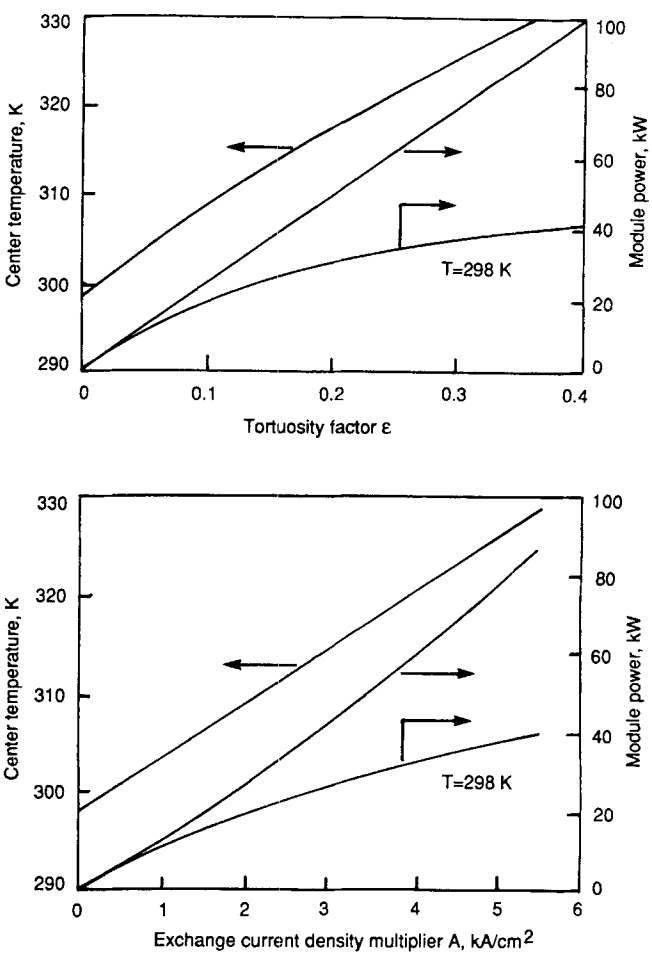

Figure 9. Center temperature and power after 1,800 s of discharge vs. tortuosity factor ϵ (top, see Eq. A4); cell exchange current density multiplier *A* (bottom, see Eq. A7).

Calculations of the power density using temperature-independent system properties evaluated at $T = 298$ K are also shown.

one expects to see the center temperature and module power rise rapidly as the module voltage is decreased from its equilibrium value, yielding large discharge currents and more irreversible heating. This is seen to be the case in Figure 8, where the module's center temperature and power are plotted against the module voltage. These results demonstrate clearly the need to consider the influence of temperature on the current-density and cell power calculation. Large voltage displacements away from the equilibrium voltage are seen to promote a thermal runaway. The dashed curves show the calculated power if the system properties are held at their ambient temperature values (298 K):

$$\text{Module power, 298 K} = V_{\text{stack}}\sigma_x\left(NU - \frac{V_{\text{stack}}}{\mathfrak{L}_x}\right)N_{\text{stack}}(2L_z)(2L_y), \quad (23)$$

which utilizes Eq. 11 for the current density of each cell. In Eq. 23, both σ_x and U are evaluated at 298 K. The dashed curves diverge from the model calculations (solid curves) at higher discharge voltages, when the temperature dependence of the system properties becomes more important. The curves labeled with $A = 5.49$ correspond to the base-case values, while those labeled with $A = 0.549$ are indicative of a degraded interface and a higher overall resistance to the cell reaction. For the same module power, the degraded interface is seen to promote a higher module center temperature, as would be expected in view of the increased irreversibilities. Note that for module voltages greater than $NU = 94.5$ V, the module power is negative, reflecting module charging. Because the cell reaction is taken to be isentropic, the module is seen to heat on both charge and discharge. The minimum temperature corresponds to that of the surroundings (298 K) and occurs when $V_{\text{stack}} = NU$.

As noted in the discussion of Figure 3, two cell features that may vary substantially in the processing of cells are the electrolyte conductivity and interfacial resistance. The two panels in Figure 9 allow one to assess the importance of such variations after 1,800 s of discharge. Shown in the top panel

are the module's center temperature and power for various electrolyte tortuosity factors ϵ (Eq. A4). Note that by the definition employed, larger tortuosity factors indicate a higher porosity polymer electrolyte and lower ionic resistance. The bottom panel displays an analogous plot for various cell exchange current density multipliers A (Eq. A7). In both plots, the curve labeled $T = 298$ K corresponds to the module power if all system properties are evaluated at 298 K and held constant. First, note that as the cell resistance is decreased, both the module power and center temperature increase. This is to be expected: the module's potential is fixed, and the lower resistances yield larger current flows, more Joule heating, and higher module temperatures. Second, the results can be used to show that neglecting the influence of property variations with temperature yields module-power calculations that are incorrect by over a factor of two. Last, note that for the constant property results, the influence of reducing exclusively the electrolyte or interfacial resistance becomes less pronounced as the resistance in question becomes small relative to other resistances in the system. Similar behavior is seen for the variable property results, but unreasonably high temperatures and powers are manifest when the behavior becomes evident.

As discussed in the context of Figure 4, a four-module battery pack is of interest for electric-vehicle applications. If such a design were to be realized, then one would expect the heat transfer from adjacent module surfaces to be reduced substantially, an effect investigated in Figure 10, corresponding to 1,800 s of discharge and the values given in Table 1. Placing the modules next to each other, so that the surfaces at $z = 0$ and $2L_z$ cannot effectively release heat, serves to increase the center temperature by a few degrees only, but the module power is increased by about 15 percent. These results again underscore the nonlinear relation between the module power and temperature. The effect of altering the convective heat-transfer coefficient uniformly for all module surfaces over the range of values typical for forced-convection heat transfer (Kreith, 1973) is presented in Figure 11. Three different exchange current density multipliers are investigated. In both Figures 10 and 11, it is shown that reducing the convective heat-transfer coefficient h serves to heat the module, reduce internal charge-transport and electrochemical-reaction resistances, and increase the module power.

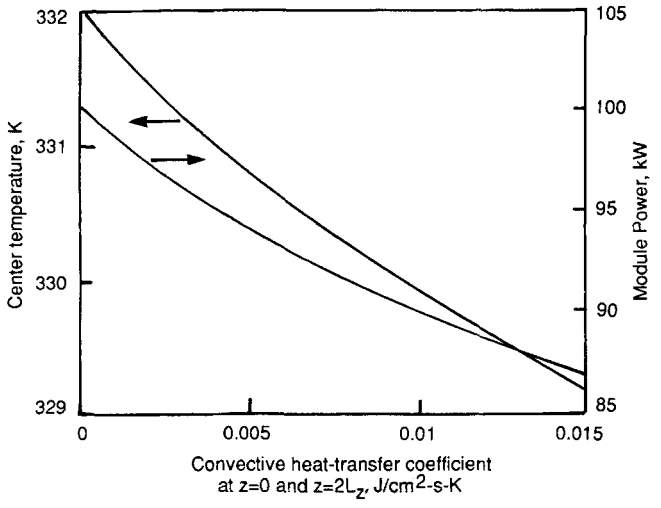

Figure 10. Center temperature and power vs. the convective-heat-transfer coefficient associated with the module surfaces $z = 0$ and $2L_z$.

The discharge time is 1,800 s.

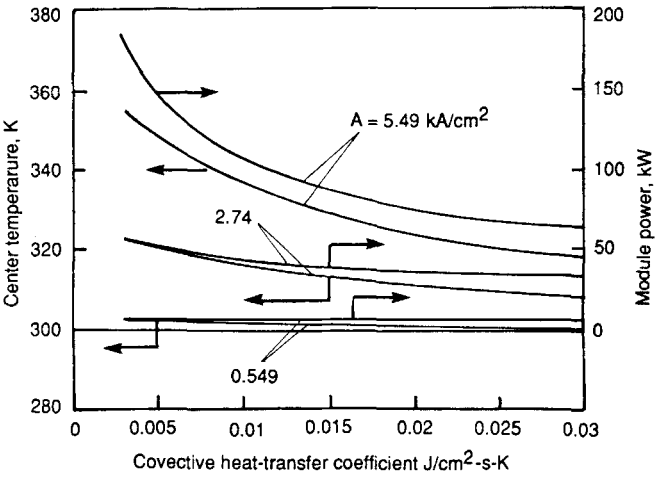

Figure 11. Center temperature and power vs. the convective heat-transfer coefficient, which is taken to be identical for all module surfaces.

Three different exchange current density multipliers A (Eq. A7) are investigated. The discharge time is 1,800 s.

Conclusion

A procedure is suggested for deriving partial differential equations that allow one to model a battery system, containing a large number of cells, and treat simultaneously the temperature and current distributions. Data taken on metallic lithium/polymer electrolyte/vanadium oxide cells, of interest for electric-vehicle applications, indicate that the cell entropy of reaction is small, and that battery modules formed from such cells can be expected to heat on both charge and discharge under normal operation. The effect of temperature on the various cell resistances results in a nonlinear current-voltage relation for a battery module. Thus as a battery is discharged at high rates, the central region of the module, which is the least accessible portion of the system to transfer heat to the cooler surroundings, becomes less resistive to current passage due to the heat generated from irreversibilities associated with transport and kinetic processes. A larger fraction of the cell current is channeled through the central portion of the module, leading to larger total currents if the battery voltage is held constant and further reducing the module resistance. If not recognized in design and operation, these phenomena can lead to thermal runaway.

Acknowledgment

The problem statement and system dimensions arose out of work with Carl Richwine (AC Delco Systems Division, General Motors Corporation), who also provided the data shown in Figure A1, which were taken from cells produced by the Valence Technology Corporation. The author owes a debt of gratitude to Dawn Bernardi (Physical Chemistry Dept., General Motors Research and Development Center) for help in both technical and expositional aspects of this work.

Notation

A = exchange current density multipliers (Eqs. A5 to A7), A/cm^2
$\hat{c}_p$ = specific heat at constant pressure, J/g·K
C = macroscopic heat capacity, $N\Sigma_{i=a,c,e}\,\ell_i\,\rho_i\hat{c}_{pi}$, J/cm^3·K
F = Faraday's constant, 96,487 C/equiv.
h = convective heat-transfer coefficient, J/cm^2·s·K
ΔH = enthalpy of reaction, J/mol
ΔH_o = enthalpy of activation at zero polarization (Eq. A5), J/mol
i = current density, A/cm^2
i_o = exchange current density, A/cm^2
I = current, A
$\underline{\underline{k}}$ = thermal conductivity, J/cm·s·K
ℓ = component (if subscripted) or cell thickness, cm
$\mathfrak{L}$ = stack dimension, cm
L = module dimension, cm
L_N = Lorenz number
n = number of electrons in reaction
$\underline{n}$ = unit normal vector pointing into the module (or stack)
N = cells per length x, cm^{-1}
N_{stack} = stacks per module
q^c = conductive heat flux, J/cm^2
$\overline{Q}$ = rate of heat transfer into the system, W
R = gas constant, 8.3143 J/mol·K
ΔS = entropy of reaction, J/mol·K
t = time, seconds
T = temperature, K
U = cell open-circuit potential, V
V = potential, V
x = coordinate (Figure 2), cm
y = coordinate (Figure 2), cm
z = coordinate (Figure 2), cm

Greek letters

ϵ = tortuosity factor (Eq. A4)
θ = polymer void fraction
ρ = mass density, g/cm^3
$\underline{\underline{\varrho}}$ = charge resistivity, Ohm·cm
$\underline{\underline{\sigma}}$ = charge conductivity, S/cm

Subscripts and superscripts

a = anode (on discharge)
c = cathode (on discharge)
e = electrolyte
i = index denoting a, c, or e
w = index denoting x, y, or z
x = x direction
y = y direction
z = z direction
∞ = surrounding environment

Literature Cited

Abraham, K. M., J. L. Goldman, and M. D. Dempsey, "Rechargeable Lithium/Vanadium Oxide Cells Utilizing 2Me-THF/LiAsF$_6$," *J. Electrochem. Soc.*, **128**, 2493 (1981).

Agar, J. N., "Thermogalvanic Cells," *Advances in Electrochemistry and Electrochemical Engineering*, Vol. 3, P. Delahay and C. W. Tobias, eds., Wiley-Interscience, New York (1963).

Bernardi, D., E. Pawlikowski, and J. Newman, "A General Energy Balance for Battery Systems," *J. Electrochem. Soc.*, **132**, 5 (1985).

Bernardi, D. M., H. Gu, and A. Y. Schoene, "Two-Dimensional Mathematical Model of a Lead-Acid Cell," *J. Electrochem. Soc.*, **140**, 2250 (1993).

Bird, R. B., W. E. Stewart, and E. N. Lightfoot, *Transport Phenomena*, Wiley, New York (1960).

Brian, P. L. T., "A Finite-Difference Method of High-Order Accuracy for the Solution of Three-Dimensional Transient Heat Conduction Problems," *AIChE J.*, **7**, 367 (1961).

Bruggeman, D. A. G., "Berechnung Verschiedener Physikalischer Konstanten von Heterogenen Substanzen: I. Dielektrizitätskonstanten und Leitfähigkeiten der Mischkörper aus Isotropen Substanzen," *Annalen der Physik*, **24**, 636 (1935).

Butler, J. N., D. R. Cogley, and J. C. Synnott, "Effect of Water on the Kinetics of the Solid Lithium-Lithium Ion Reaction in Propylene Carbonate," *J. Phys. Chem.*, **73**, 4026 (1969).

Chen, Y., and J. W. Evans, "Heat Transfer Phenomena in Lithium/Polymer-Electrolyte Batteries for Electric Vehicle Application," *J. Electrochem. Soc.*, **140**, 1833 (1993).

Chen, Y., and J. W. Evans, "Thermal Analysis of Lithium Polymer Electrolyte Batteries by a Two Dimensional Model—Thermal Behavior and Design Optimization," *Electrochim. Acta*, **39**, 517 (1994).

Conway, B. E., and D. P. Wilkinson, "Non-isothermal Cell Potentials and Evaluation of Entropies of Ions and of Activation for Single Electrode Processes in Non-aqueous Media," *Electrochim. Acta*, **38**, 997, 1993.

Doyle, M., T. F. Fuller, and J. Newman, "Modeling of Galvanostatic Charge and Discharge of the Lithium/Polymer/Insertion Cell," *J. Electrochem. Soc.*, **140**, 1526 (1993).

Dudley, J. T., D. P. Wilkinson, G. Thomas, R. LeVae, S. Woo, H. Bolm, C. Horvath, M. W. Juzkow, B. Denis, P. Juric, P. Aghakian, and J. R. Dahn, "Conductivities of Electrolytes for Rechargeable Lithium Batteries," *J. Power Sources*, **35**, 59 (1991).

Epelboin, I., M. Froment, M. Garreau, J. Thevenin, and D. Warin, "Behavior of Secondary Lithium and Aluminum-Lithium Electrodes in Propylene Carbonate," *J. Electrochem. Soc.*, **127**, 2100 (1980).

Fauteux, D., and R. Koksbang, "Rechargeable Lithium Battery Anodes: Alternatives to Metallic Lithium," *J. Appl. Electrochem.*, **23**, 1 (1993).

Fuller, T. F., M. Doyle, and J. Newman, "Relaxation Phenomena in Lithium-Ion-Insertion Cells," *J. Electrochem. Soc.*, **141**, 982 (1994).

Gosden, D. F., "Battery Requirements for Electric Vehicles," *J. Power Sources*, **45**, 61 (1993).

Harned, H. S., and B. B. Owen, *The Physical Chemistry of Electrolytic Solutions*, 3rd ed., Rienhold, New York (1958).

Jakob, M., *Heat Transfer*, Vol. I, Wiley, New York (1949).

Jasinski, R., "Electrochemistry and Application of Propylene Carbonate," *Advances in Electrochemistry and Electrochemical Engineering*, Vol. 8, P. Delahay and C. W. Tobias, eds., Wiley-Interscience, New York, p. 253 (1971).

Jorné, J., and C. W. Tobias, "Electrode Kinetics of the Alkali Metals in $AlCl_3$-Propylene Carbonate Solution," *J. Electrochem. Soc.*, **121**, 994 (1974).

Kim, J., T. V. Nguyen, and R. E. White, "Thermal Mathematical Modeling of a Multicell Common Pressure Vessel Nickel-Hydrogen Battery," *J. Electrochem. Soc.*, **139**, 2781 (1992).

Klincewicz, K. M., and R. C. Reid, "Estimation of Critical Properties with Group Contribution Methods," *AIChE J.*, **30**, 137 (1984).

Kreith, F., *Principles of Heat Transfer*, 3rd ed., Ser. in Mechanical Engineering, Harper and Row, New York, p. 14 (1973).

Lee, J., K. W. Choi, N. P. Yao, and C. C. Christianson, "Three-Dimensional Thermal Modeling of Electric Vehicle Batteries," *J. Electrochem. Soc.*, **133**, 1286 (1986).

Meibuhr, S. G., "Electrode Studies in Nonaqueous Electrolytes: I. The Lithium Electrode in $LiClO_4$-Propylene Carbonate Solutions," *J. Electrochem. Soc.*, **117**, 56 (1970).

Meibuhr, S. G., "Electrode Studies in Nonaqueous Electrolytes: II. Anion Effect on the Kinetics of Li/Li$^+$ in Propylene Carbonate," *J. Electrochem. Soc.*, **118**, 1320 (1971).

Morse, P. M., and H. Feshbach, *Methods of Theoretical Physics*, Part I, McGraw-Hill, New York (1953).

Morzilli, S., F. Bonino, and B. Scrosati, "Characteristics of the Lithium Electrode in Organic and Polymeric Electrolytes," *Electrochim. Acta*, **32**, 961 (1987).

Newman, J., and W. Tiedemann, "Porous-Electrode Theory with Battery Applications," *AIChE J.*, **21**, 25 (1975).

Odziemkowski, M., and D. E. Irish, "An Electrochemical Study of the Reactivity at the Lithium Electrolyte/Bare Lithium Metal Interface," *J. Electrochem. Soc.*, **139**, 3063 (1992).

Ortega, J. M., and W. C. Rheinboldt, *Iterative Solution of Nonlinear Equations in Several Variables*, Computer Science and Applied Mathematics Series, Academic Press, New York (1970).

Perry, R. H., and C. H. Chilton, eds., *Chemical Engineers' Handbook*, 5th ed., McGraw-Hill, New York (1973).

Ratkje, S. K., T. Ikeshoji, and K. Syverud, "Heat and Internal Energy Changes at Electrodes and Junctions in Thermocells," *J. Electrochem. Soc.*, **137**, 2088 (1990).

Reid, R. C., J. M. Prausnitz, and B. E. Poling, *The Properties of Gases and Liquids*, 4th ed., McGraw-Hill, New York (1987).
Richtmyer, R. D., and K. W. Morton, *Difference Methods for Initial-Value Problems*, 2nd ed., No. 4, Interscience Tracts in Pure and Applied Mathematics Ser., Wiley-Interscience, New York (1967).
Riezenman, M. J., "Electric Vehicles," *IEEE Spectrum*, p. 18 (Nov. 1992).
Scarr, R. F., "Kinetics of the Solid Lithium Electrode in Propylene Carbonate," *J. Electrochem. Soc.*, **117**, 295 (1970).
Scarr, R. F., "Alkali Metals," *Encyclopedia of Electrochemistry of the Elements*, Vol. IX, part B, A. J. Bard, ed., Marcel Dekker, New York (1986).
Scrosati, B., "Lithium Rocking Chair Batteries: An Old Concept?" *J. Electrochem. Soc.*, **139**, 2776 (1992).
Shen, D. H., and G. Halpert, "Design Concepts of High Power Bipolar Rechargeable Lithium Battery," *J. Power Sources*, **43–44**, 327 (1993).
Takehara, Z., et al., "Thin Film Solid-State Lithium Batteries Prepared by Consecutive Vapor-Phase Processes," *J. Electrochem. Soc.*, **138**, 1574 (1991).
Yde-Andersen, S., R. Koksbang, and J. S. Lundsgaard, "Rechargeability and Rate Capability of Polymer Electrolyte Batteries at Different Temperatures," *Solid State Ionics*, **53–56**, 673 (1992).
Yeast, R. C., Editor, *CRC Handbook of Chemistry and Physics*, 58th ed., (1987–1988).
Yu, D., W. Qiu, and Q. Liu, "Ambient-Temperature Polymer Electrolyte Secondary Li/V_6O_{13} Battery," *Synthetic Metals*, **47**, 1 (1992).
Verbrugge, M. W., and B. J. Koch, "Microelectrode Investigation of Ultrahigh-Rate Lithium Deposition and Stripping," *J. Electroanal. Chem.*, **367**, 123 (1994).
Verbrugge, M. W., "Primary Current Distribution in a Thin-Film Battery. Application to Power-Density Calculations for Lithium Batteries," *J. of Electrostatics*, **34**, 61 (1995).

Appendix: Parameters and Properties

Charge conductivities

Since the electrical conductivities of lithium and carbon (in the insertion electrode) are many orders of magnitude greater than the ionic conductivity of the propylene carbonate–based electrolyte, the majority of the ohmic resistance to x-directed current flow is due to the electrolyte resistance.

The temperature dependence of the lithium and carbon electronic conductivities was estimated by assuming a constant Lorenz number N_L (Jakob, 1949; Bird et al., 1960), which can be expected to work well for metallic conductors:

$$N_L = \frac{k}{\sigma T}. \tag{A1}$$

Thermal and electronic conductivity data (Yeast, 1987–1988) yield Lorenz numbers of

$$(N_L)_{Li} = (N_L)_{\text{anode}} = 26.9\times 10^{-9}\ \text{V}^2/\text{K}^2 \tag{A2}$$

$$(N_L)_{C} = (N_L)_{\text{cathode}} = 755\times 10^{-9}\ \text{V}^2/\text{K}^2. \tag{A3}$$

Using the thermal conductivity expressions described below, we obtain anode and cathode temperature-dependent conductivity expressions ($\sigma = k/N_L T$).

The ionic conductivity of the propylene carbonate–based electrolyte is described by

$$\sigma_e = \epsilon A_o \exp\left(-\frac{E_A}{RT}\right), \tag{A4}$$

where the Bruggeman (1935) tortuosity factor ϵ for the polymer matrix is $\epsilon = \theta^{1.5} = 0.35$, which is based on a porosity θ of 0.5. The solvent-phase conductivity is taken to correspond to 1 M $LiAsF_6$ in propylene carbonate, yielding $A_o = 8.53$ S/cm and $E_A = 4.34$ kcal/mol (Dudley et al., 1991).

Exchange-current densities

The stability of the lithium-electrolyte interface has hindered the commercial success of secondary lithium batteries, and the wide variance in the reported exchange current densities (Jasinski, 1971) for the Li-Li^+ reaction reflects the complex nature of the associated interface. One can speculate that the fundamental electron-transfer reaction at the insertion electrode differs from that of the lithium electrode primarily because of the reduced activity of Li^0 in the insertion electrode environment. Thus in the results section, the effect of varying the exchange current density is explored, and the reaction enthalpies of the two cell electrochemical reactions are assumed to be identical. The exchange current density can be expressed as:

$$i_{oa} = A_{\text{Li-Li}^+} \exp\left(-\frac{\Delta H_o}{RT}\right). \tag{A5}$$

Meibuhr (1970, 1971) measured an enthalpy of activation at zero polarization of $\Delta H_o = 8.5$ kcal/mol. Since it is assumed that the reaction enthalpies of the two cell electrochemical reactions are identical:

$$i_{oa} + i_{oc} = (A_a + A_c)\exp\left(-\frac{\Delta H_o}{RT}\right) \tag{A6}$$

$$= A \exp\left(-\frac{\Delta H_o}{RT}\right). \tag{A7}$$

The factor A shall be referred to as the cell exchange-current density multiplier. To determine an upper bound on $A_{\text{Li-Li}^+}$, note the highest exchange current density reported for the Li-Li^+ at 298 K is 31.6 mA/cm^2 (Verbrugge and Koch, 1994), yielding $A_{\text{Li-Li}^+} = 54.9$ kA/cm^2. In general, the reported exchange current densities are typically about an order of magnitude lower than this (Butler et al., 1969; Meibuhr, 1970, 1971; Jorné and Tobias, 1974; Epelboin et al., 1980; Scarr, 1986; Morzilli et al., 1987), and a value of $A = 5.49$ kA/cm^2 was used for the base case. Various sensitivities are done in the results and discussion section that elucidate the importance of this parameter. Fauteux and Koksbang (1993) have recently reviewed the problems and prospects associated with rechargeable lithium battery anodes, with particular emphasis on alternatives to metallic lithium. Scrosati (1992) has helped to clarify the history of substitute electrodes for metallic lithium. It is a simple matter to accommodate more complex reaction expressions or alternative anodes, or both, should formulae and parameter values become available.

Thermal conductivities

Since the thermal conductivity of lithium is almost an order of magnitude greater than that of carbon, it is important to specify accurately the lithium thermal conductivity to de-

scribe thermal diffusion parallel to the electrode surfaces (in the y and z directions). Axial thermal diffusion, however, is determined primarily by the least conductive component, the polymer electrolyte. Over the temperature range of interest, the thermal conductivity of lithium and carbon are well represented by (Yeast, 1987–1988)

$$k = a - b(T - 273) \tag{A8}$$

where

Cathode	Anode
$a = 0.15$	$a = 0.859$
$b = 0.00034$	$b = 0.00042$

Sato's method (Reid et al., 1987) was used to estimate a temperature-dependent thermal conductivity for the propylene carbonate–based electrolyte:

$$k_e = \frac{(1.11/\sqrt{M})\left[3 + 20(1 - T_r)^{2/3}\right]}{3 + 20(1 - T_{br})^{2/3}} \tag{A9}$$

The critical temperature T_c for propylene carbonate is required to calculate the reduced temperature $T_r = T/T_c$ and boiling point $T_{br} = T_b/T_c$. (The boiling-point temperature is given by T_b.) Klincewicz's relation (Klincewicz and Reid, 1984; Reid et al., 1987) was used for estimating T_c:

$$T_c = 50.2 - 0.16M + T_b. \tag{A10}$$

The following parameter values were used:

$$M = 102.1 \text{ g/mol}$$
$$T_b = 515 \text{ K}.$$

Handbook (Yeast, 1987–1988) data are available for the temperature variation of propylene glycol's thermal conductivity. When Eqs. A9 and A10 are used to estimate a thermal conductivity for propylene glycol, less than a 15% difference is obtained at 80°C. The calculated thermal conductivity for propylene carbonate is very close to that of propylene glycol, as would be expected in light of their similar molecular structure.

Heat capacities and densities

The heat capacity of lithium is given by (Perry, 1973):

$$\hat{c}_{p,Li} = 0.41 + 0.011(T). \tag{A11}$$

The heat capacity of vanadium dioxide, which is quite close to that of carbon (Yeast, 1987–1988), is taken to be that of V_6O_{13}:

$$\hat{c}_{p,V_6O_{13}} = 0.87 + 8.3 \times 10^{-5}(T) - \frac{19{,}000}{T^2}. \tag{A12}$$

The Chueh-Swanson functional-group contribution method (Reid et al., 1987) was used to estimate the heat capacity of the propylene carbonate–based electrolyte. Thus the known molar heat capacity of diethyl carbonate

$$CH_3—CH_2—O—(CO)—O—CH_2—CH_3,$$

120 J/mol·K (Perry, 1973), was altered by subtracting the contributions from an end methyl group (36.8 J/mol·K) and the adjacent $—CH_2$ group (30.4 J/mol·K) and adding a —CH— contribution (21 J/mol·K) to form the ringed structure. The resulting heat capacity is 0.72 J/g·K. This method should be sufficiently accurate for our purposes since the Chueh-Swanson functional-group contribution method is known to work well for estimating alkyl group contributions, and the carbonate portion of the structure is taken from the known diethyl carbonate heat capacity. No attempt is made to account for variations in the heat capacity of the propylene carbonate–based electrolyte with temperature since liquid heat capacities do not observe a strong temperature dependence far from their boiling point, as can be seen in Fig-

Table A1. Open-Circuit Potential vs. Temperature Data

State of Charge	Open-Circuit Potential U, V
100	2.7
75	2.6
50	2.53
25	2.35

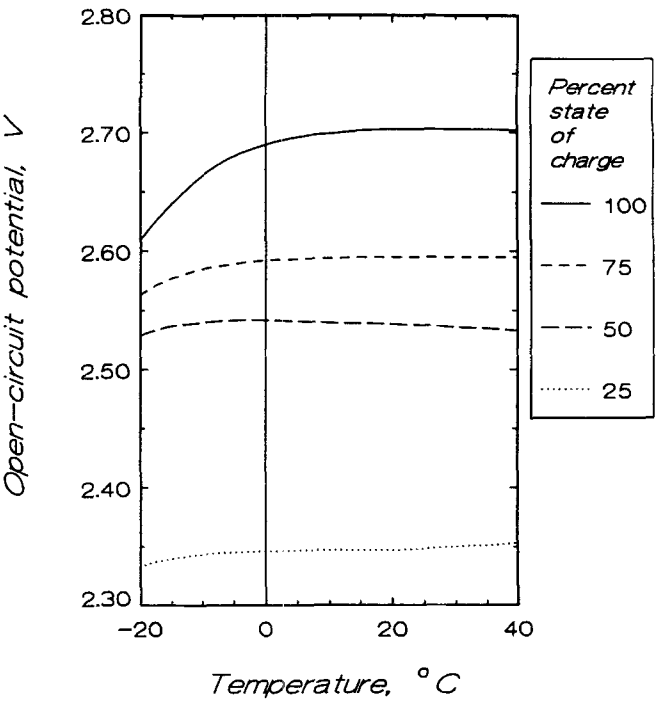

Figure A1. Open-circuit potential vs. temperature for various states of discharge.

These data were taken by Carl Richwine of the Delco Remy Division of the General Motors Corporation from cells provided by the Valence Technology Corporation. The cells were of the form: metallic lithium/polymer electrolyte/vanadium oxide.

ure 5-3 of Reid et al. (1987) or Handbook heat capacity data (Yeast, 1987–1988). A shallow minimum is often observed at temperatures just below the boiling point.

The component densities ρ_i are not strong functions of temperature and are given by:

$$\rho_{\text{anode}} = 0.53 \text{ g/cm}^3 \text{ (Yeast, 1987, 1988)}$$

$$\rho_{\text{cathode}} = 3.5 \text{ g/cm}^3 \text{ (Abraham et al., 1981)}$$

$$\rho_{\text{electrolyte}} = 1.2 \text{ g/cm}^3 \text{ (Jasinski, 1971).}$$

Thus, the macroscopic heat capacity:

$$C = N \sum_{i=a,c,e} \ell_i \rho_i \hat{c}_{pi},$$

is nearly 2 J/cm^2·K at 298 K, about one-half that of water.

Open-circuit cell potential

Open-circuit cell potential data as a function of temperature are shown in Figure A1 for four different states of charge: 100, 75, 50 and 25%. These data were taken by Carl Richwine of the Delco Remy Division from cells provided by the Valence Technology Corporation. The metallic lithium/polymer electrolyte/vanadium oxide cells are similar to those described by Yde-Andersen et al. (1992) and Yu et al. (1992). Above 0°C, no significant change in the open-circuit potential is observed. The state of charge enters the model calculations through the open-circuit potential U. To capture the primary phenomena contributing to the module's performance without introducing undue expositional complexity, all calculations were completed with a constant state of charge. For the purposes of this work, Table A1 can be taken from the data shown in Figure A1.

Manuscript received June 6, 1994, and revision received Aug. 19, 1994.